DEVELOPMENT OF X-RAY LUMINESCENCE DETECTION SYSTEM AND CHARACTERIZATION OF X-RAY IRRADIATED QUANTUM DOTS FOR IMAGE-GUIDED X-RAY PHOTODYNAMIC THERAPY

BY

BYUNG HUI YOON

THESIS

Submitted in partial fulfillment of the requirements
for the degree of Master of Science in Bioengineering
in the Graduate College of the
University of Illinois at Urbana-Champaign, 2017

Urbana, Illinois

Adviser:

Associate Professor Ling-Jian Meng

ABSTRACT

The work in this thesis demonstrates X-ray luminescence (XL) detection system setup and XL quantification of X-ray irradiated quantum dots (QDs) to study efficiencies of X-ray photodynamic therapy (X-PDT). The XL detection system utilizes a light-sensitive electron-multiplying charge coupled device (EMCCD), a demagnifying (DM) image intensifier, and on optical lens to monitor XL signal emitted from the QDs. We used core-shell QDs and doped QDs to characterize their XL properties and absorption of X-ray photons. Along with the characterization of XL, the work eventually discusses potential applications of the system as a new biomedical theranostic modality. This study also demonstrates how well-controlled synthesis parameters of QDs such as elemental composition and dopant integration foreshow mechanisms of XL. Superimposed images of optical and XL signals are also presented to show potential fluorescence microscope imaging applications. Additionally, polydimethylsiloxane (PDMS)-based optical phantom with scattering medium was fabricated to reproduce tissue-mimicking optical property in XL computed tomography (XLCT) study.

To My Father and Mother

ACKNOWLEDGMENTS

I would first like to thank my colleagues, Jonathan George, Luca Giannoni, Andrew Groll, Dan Strat, Elena Zannoni, Xiaochun Lai, and Mohan Li for their advices and cheers towards my research. I would also like to express my gratitude to my advisor, Professor Ling-Jian Meng, who helped me make this work possible. He consistently helped me correct my own mistakes whenever I fell into pitfalls or had a question about my research. I would also like to thank Professor Andrew Smith and Doctor Sung Jun Lim on their continued supports for materials property research. I would like to extend my appreciation to Professor Patrick La Riviere from the University of Chicago for his feedback. Finally, I must express my sincere affection and gratitude to my parents and friends for providing me boundless support and encouragement. Thank you.

TABLE OF CONTENTS

Chapter 1: Introduction

Accurate diagnoses of disease are essential and important in clinics. Medical imaging has played a significant role in diagnoses and medicine since Dr. Wilhelm Röntgen discovered X-rays in 1895 [1]. Over the century, X-ray imaging has grown into more mature modalities such as radiography, X-ray Computed Tomography, angiography, X-ray fluoroscopy, and digital X-ray projection imaging with contrast agent. X-ray system, owing to its clinical efficacy and reasonable price, is widely available in clinical settings for diagnoses of bone fracture which is the biggest problem caused by bone disease. Also, among population that is age 65 and older, bone fractures are the most common musculoskeletal disease that requires hospitalization [2]. Hence, the use of X-ray imaging system will be more demanding as the number of aging population increases worldwide, implying X-ray technique is very accessible as a newly-developed component of hybrid modalities.

Complex optical imaging systems such as optical coherence tomography (OCT) or diffuse optical tomography (DOT) have advanced in medicine but it is challenging for such systems to scan inhomogeneous whole-body or organs. While the optical systems are not commonly available in primary care environments, a simple-formatted pulse oximeter which uses red-infrared light absorption technique is readily available [3]. In medical imaging, what makes complex optical imaging systems challenging to play important roles are their limited practicality. Such limitations include optical photons' short penetration depths, autofluorescence of tissue, and lack of sufficiently sophisticated reconstruction model [4]. However, certain optical systems are well-known for high spatial resolution as well as good coordination with fluorescence probes such as quantum dots or fluorescein.

Cancer has been one of the many diseases that have not been conquered. Radiotherapy as well as chemotherapy are gold standards of treating cancer non-invasively but they are known to induce many side-effects due to their low specificity. Surgical removal of tumor is another gold standard of preventing cancer from spreading over body. Conventional targeted anticancer drugs have little treatment outcomes with some exceptions and the number of FDA-approved drugs are significantly low [5]. Optical photodynamic therapy excels in its sensitivity and specificity to

treatment of cancer but penetration depth of the therapy is limited. With X-ray induced photodynamic therapy (XPDT), depth limitation can be overcome and even combined with radiotherapy with low dosage. Hence, there is a need (1) to develop a system that can detect XPDT mechanisms, and (2) to characterize potential X-ray photosensitizer.

A medical imaging system that has advantages of both X-ray and optical system is ideal in that each system can be complementary. X-ray beam has deep penetration depth through tissue. X-ray energy spectrum detection system shows specifically what elements are present in picogram level [6]. Optical detection system has high spatial resolution in sub-cellular level. To accommodate these advantages, a hybrid system of X-ray fluorescence computed tomography (XFCT), X-ray luminescence computed tomography (XLCT), X-ray computed tomography (CT), and X-ray spectrometer is developed in this study. In addition to development of the system, X-ray irradiated QDs were characterized for their X-ray fluorescence and X-ray luminescence properties to enhance sensitivity of the system.

1.1 X-ray Fluorescence of Atoms

X-ray fluorescence (XRF) occurs within a single atom. Each atom has electron clouds around the nucleus. Electrons that are orbiting on the first shell of clouds are called K-shell electrons, those on the next consecutive shells are L-shell electrons, M-shell electrons, and so on. Once X-ray photon collides with the electrons, the energetic photon knocks out inner shell electrons (K, L, or M). Incident X-ray photon must have energy that exceeds binding energy between inner shell electron and nucleus. To fill the hole that is produced by vacancy of the electron, another electron in outer shell relaxes to fill the vacancy, emitting X-ray photon. For example, if K-shell electron is knocked out, L-shell electron relaxes. The X-ray photon emitted from the transition is called K X-ray. XRF yield is relatively high. For elements with atomic number larger than 78, XRF yield becomes greater than 95% [7]. Due to different orbital configurations, each element has different K and L energies, allowing detection of different metals in cells and chemicals.

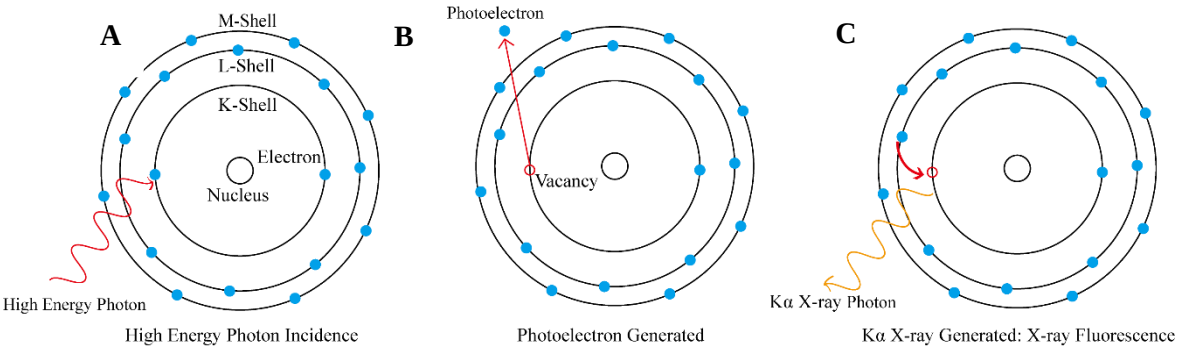

Figure 1.1 Consecutive processes of XRF. (A) High energy photon is incident. (B) Electron orbiting inner core shell (K-shell) is ejected, leaving a vacancy or a core hole. (C) Electron orbiting L-shell recombines with the core hole, generating characteristic Kα X-ray.

1.2 Scintillation and X-ray Excited Optical Luminescence of Nanocrystals

Scintillation mechanisms of inorganic crystals start with incidence of high energy photons such as X-ray photons or gamma ray photons. There are various scintillation models on recombination of high energy excitons (electrons and holes). One of the major models starts with incidence of high energy photons such as X-ray photons or gamma ray photons. Electrons from the core band of atoms are excited and reside conduction band of the molecule or crystal. The newly generated hot electrons and holes start colliding with other electrons and holes via inelastic collision. Finally, multiple electrons and holes which gathered on conduction and valence band recombine, generating multiple visible photons [8].

X-ray excited optical luminescence (XEOL) or X-ray luminescence (XL) is thought to be a similar process as scintillation is. However, mechanisms and quantum efficiencies differ between those of bulk scintillation and those of nanocrystals as there are more chance of nanocrystals to quench or lose energies to surrounding environment. Hence, development of XEOL nanocrystals required close look at spectroscopic properties. In this study, the term XEOL is equivalent to XL.

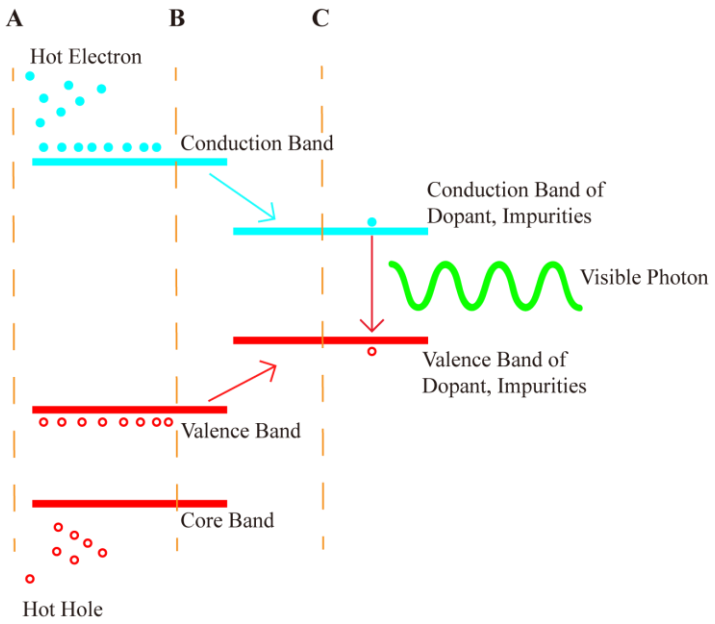

Figure 1.2 Mechanism of high energy scintillation. (A) Hot exciton (Pair of electron and hole) is generated. Cascades of electrons and holes occur, gathering multiple electrons and holes near conduction band and valence band. (B) Excitons transport to conduction and valence band of dopant or impurities. (C) Excitons radiatively recombine and emits visible photons.

1.3 Quantum Dots as Unique XEOL Nanocrystals

Quantum dots (QDs) are nanometer-sized semiconductor nanocrystals that are used in different fields extending from biological research to television industries. QDs are interesting nanocrystals in that their physical properties are determined by quantum confinement effect so it is appropriate to probe fundamentals of quantum mechanics [9]. Over decades, their syntheses methods have been developed for controlled physical properties, resulting in well-controlled parameters such as reaction temperature, shell thickness, structure, and elemental composition. This allows synthesis parameters to change relatively easier than those of conventional lanthanide XEOL nanocrystals. Hence, QDs are unique XEOL nanocrystals that are appropriate in characterizing XL with different physical parameters.

1.4 Limitations of the Study

Due to building restriction of handling live animals, some sample was prepared with silicon phantoms to mimic optical properties of human tissue. While UV-Vis spectroscopic information

is strictly measured, X-ray spectroscopic information of QDs and its connection to optical spectrum are weakly described. Further studies on where X-ray excited electrons travel to eventually recombine with X-ray generated holes should be closely analyzed.

1.5 Impact of the Study and Potential Applications

The nature of visible light makes conventional photodynamic therapy challenging to penetrate through deep tissue that is more than 1cm thick. X-ray activated photosensitizers or X-ray activated scintillator-photosensitizer complex may overcome this hurdle along with therapeutic effects of X-ray radiotherapy. Developed XL system combined with X-ray spectrometer helps understand spectroscopic properties of nanoparticles and their energy transfer mechanism in generation of reactive oxygen species. Fast and sensitive XL detection system will allow quantifications of dim luminescence and phosphorescence detection via intensified silicon-based CCD sensor.

Quantification of reactive oxygen species has not been studied extensively for direct applications of X-ray photodynamic therapy. For example, XRF, XL, and photosensitizing effects of QDs may be related and this study may help understand correlation among them. QDs-embedded X-ray screen can be developed for low-dosage and sensitive X-ray system [10]. QDs-embedded solar panels may harvest not only UV-VIS range but also cosmic X-ray and even gamma ray for wider range of photon harvesting. Hence, the impact of this study is towards wide variety of fields including biomedical engineering, materials science, radiological engineering, and physics.

1.6 Overview

The thesis is composed of six different chapters that describe development of idea, analysis of data, and characterization of results. Chapter 2 reviews published literature. This chapter describes various applications of XL system, characterizations of QDs under high energy source, biological applications of synchrotron and benchtop XF system, and various studies on mechanisms of XF, XL, and Auger recombination. Chapter 3 discusses the methods used in the research for detection of XL, XF, and transmitted X-ray. It defines system components and chemicals used for investigation of XL and XF. Chapter 4 revisits contents of chapter 4 and

describes the obtained results of XL quantification as well as imaging were acquired. Chapter 5 describes conclusions based on results that were acquired from the hybrid system data such as XL, XF, and CT. Chapter 6 discusses potential applications on how XF and XL may be applied, experimental setup that was designed but not conducted, potential mechanisms of how XL is generated, and possible improvements of the hybrid system in the future.

Chapter 2: Literature Review

There have been numerous studies on XL imaging, X-ray fluorescence imaging, characteristics of ionized nanoparticle, and applications of these techniques at once. Such applications contain deeper understandings of physical chemistry as there are much mystery present in energetic excitations regime of nanoparticles. Hence, a close look at spectroscopic studies on high energy excitations, and emission is extremely important as there may be plenty of parameters that are missing for efficient synthesis of the nanoparticles.

2.1 History of Quantum Dots and Quantum Dots as Diagnostic Imaging Probes

The characterization and development of QDs have been extensively done since their first discovery in 1982 by a Russian scientist Alexey Ekimov [11]. CuCl QDs were first discovered in the form of glass dopants. Quantum confinement effect of which explains change in absorption spectra with changing average radii was observed. Over the last few decades, physics and chemistry of the semiconductor nanocrystals have been explored for their effective use in biology, solid state physics, molecular imaging, and biosensing. Their superiority in utilization as cellular imaging probes have been excellently reviewed by S. Nie and A.M. Smith [12]. With QDs, biodistribution study, toxicology study, and molecular tagging of organelles were possible.

2.2 Recombination Mechanisms of Quantum Dots under Ionizing Radiation

Initial characterization of QDs under ionizing radiation such as alpha particle, X-ray, and gamma ray were done by S.E. Letant and T.F. Wang (2006) [13, 14]**.** For this study, porous VYCOR glass slab was prepared by hydrofluoric acid etching to increase porosity of the glass matrix. Once the slab is etched, CdSe/ZnS core-shell QDs (Emission: 510nm) were embedded to the matrix. 1/16 in. thick sample was placed in front of a photomultiplier tube (PMT) and 1μCi ^{241}Am was used as gamma source. 15% of energy resolution at 59keV was yielded, which is two times higher energy resolution than that of NaI scintillator (30% at 59keV). However, scintillation data of QDs nanocomposite were acquired for 3 days due to their low concentrations.

Researchers have also investigated improving high energy quantum efficiencies of QDs via energy transfer mechanisms between matrix material and QDs. M. Hossu et al. (2012) [15]

synthesized CdTe/LaF3:Ce nanocomposites via wet-chemistry method. Energy transfer mechanism was utilized to compensate low stopping power of CdTe QDs. Approximately six times higher intensity of XL at peak wavelength were achieved with the nanocomposites. W.G. Lawrence et al. (2012) [16] incorporated CdTe QDs in polyvinyl alcohol (PVA) and CdSe QDs in polystyrene under 8keV X-ray generator with operating tube voltage at 40kV and tube current at 20mA (Cu target). Next, 2,5-diphenyl oxazole (PPO) and 1-4,bis-2-(5-phenyloxazolyly)-benzene (POPOP) that are known as organic scintillators were incorporated for increasing chance of harvesting excitons. With such incorporation, number of excitons that are lost through non-radiative decays decreased, leading higher scintillation quantum efficiency of QDs. For characterization of emission wavelengths, PMT combined with monochromator was used. On their emission spectrum of solution phase CdSe QDs, not only main emission peak is present but also minor emission peaks are present, foreshowing different relaxation mechanisms may have occurred.

G. Gaur et al. (2016) [17] found that optical properties of QDs after irradiation of high energy source are altered due to degradation of ligands. For example, ionization of QDs changed their photoluminescence intensity and fluorescence lifetime. Radiation-induced damage reduced lifetimes of exciton and increased photooxidtation. Exposure to free-thiols solution to damaged QDs surface recovered photoluminescence, proving the surface treatment is essential for reforming a CdS shell.

Carrier population statistics and relaxation pathways of electron-hole pairs (excitons) of QDs have been extensively studied by V.I. Klimov and M.G. Bawendi [18]. Physics of semiconductor in the regime of bandgap energy has been well-established and population statistics is relatively well-known. However, with incident energy that is larger than bandgap, different spectral yield as well as fluorescence lifetime occur, implying unconventional relaxation mechanisms may be present. V.I. Klimov (2014) [19] explains such peculiar relaxation mechanisms with multiple exciton generation (MEG) or carrier multiplication (CM). Once colloidal QDs are excited by incident energy that is larger than $2.5E_g \sim 3E_g$ where E_g is a bandgap energy, multiple excitons as well as charged excitons are generated around conduction and valence band.

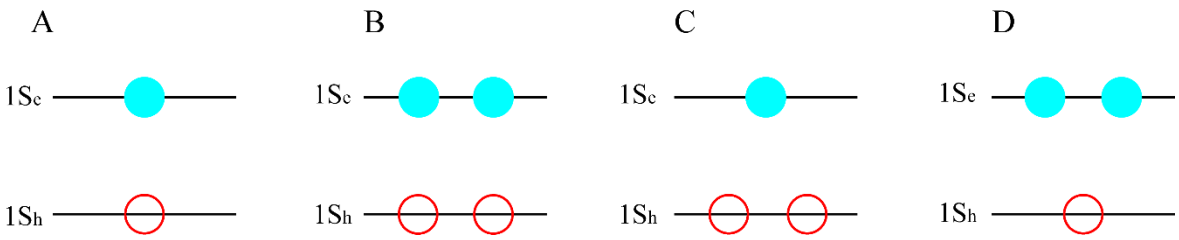

Figure 2.1 Different carrier multiplication (CM) scenarios under high energy excitations. $1S_h$ denoted first energy state of holes and $1S_e$ denotes first excited energy state of electrons. (A) Single exciton is described one pair of hole and electron. (B) Biexciton is depicted as two pairs of hole and electron. (C) Positively charged Trion is described as two holes and one electron. (D) Negatively charged Trion is described as one hole and two electrons.

Figure 2.1 depicts different scenarios of CM under high energy excitations. Due to coulomb interactions of carriers that have same charge, MEG with larger number of excitons tends to have faster decaying dynamics yet weaker intensities. According to the L.A. Padilha et al. (2013), time-resolved photoluminescence data of CdSe/ZnS nanocrystal film, high fluence laser also pumps number of multiexcitons [20]. Based on these characteristic studies, Klimov successfully resolve multiexciton dynamics in both transient and spectral cathodoluminescence analyses of QDs at 20keV picosecond electron pulses.

2.3 X-ray Luminescence Computed Tomography

XLCT has become an emerging field of interest due to development of nanophosphors as well as less amount of unwanted nonspecific optical signal (G. Pratx et al. 2010) [21]. Conventional optical fluorescence imaging has notorious noise autofluorescence signal that is originating from light-excited tissue fluorescence. The unique system geometry proposed by G. Pratx et al. (2010) allows both X-ray phase imaging and XLCT so that molecular and anatomical imaging would be viable.

Reducing radiation dose is another challenge in imaging. D. Chen et al. (2013) [22] used cone beam X-ray to reduce scanning time of XLCT, enhancing practical application of the technique. D. Chen et al. (2015) [23] also proposed a depth related adaptive regularized split Bregman (DARSB) method of XLCT to reduce location error to 1.1 mm in both simulations and phantom experiment. However, reconstruction results of the experiments showed relatively blurrier image compared to traditional CT images done in radiological imaging modalities.

2.4 X-ray Fluorescence and X-ray Fluorescence Computed Tomography

XRF is a useful technique that measures elemental information as well as quantitative analysis of certain elements. The technique has been used for characterizing different types of samples for studies in spectroscopy, crystal analysis, chemical analysis, botany, and environmental science. It is exceptionally beneficial to use in elemental analysis in that the technique has excellent sensitivity down to picogram level (L.J. Meng et al. 2011) [6]. With the developments of high fluence narrow beam X-ray optics, 100 nm of spatial resolution could be achieved (S. Corezzi et al. 2009) [24].

Energy selective characteristic of XRF essentially allows multispectral imaging of different metals as well as metal ions with high specificity and good resolution. S. Corezzi et al (2009) reported synchrotron-based X-ray fluorescence imaging of SKOV3 cancer cells and β-tubulin with HER2-targeted CdSe QDs. Selenium XRF imaging map (density: 4 to 8 X 10^{-20} g of Se per pixel) suggested that Se is a good marker for detecting QDs in a biological sample as other characteristic X-ray fluorescence peaks of biologically relevant element do not overlap with Kα Se line.

Glass or quartz products are frequently used to fix biological samples because such products have exceptional transmission rate in optical photons and are resistant to chemicals. However, introduction of contaminants in fabricating glass/quartz products is inevitable. To avoid from detecting X-ray fluorescence of such contaminants, E. Vergucht et al. (2015) reported first in vivo X-ray fluorescence imaging of microalgae manipulated by optical-tweezers [25]. The reported results show that presence of Cu-Ni, or Cu-Zn metal mixtures enhance toxic effects of Cu.

XRF imaging can also detect endogenous metals that are naturally present in a human body. Such metals may be hints for growing tumor in a human body. L. Finney et al. (2007) reported that copper was present in high concentrations in areas where branching morphogenesis may be active [26]. The experiment particularly exploited XRF imaging to image copper present in human breast-infiltrating ductal carcinoma tumor tissues. The study has found copper addition to a cell can initiate angiogenesis.

NAMI-A and KP1019 are Ruthenium-containing anticancer drugs that have entered clinical trials. S. Antony et al. (2013) reported tracking of these drugs in a single human cancer cells to track cellular uptake of the drugs [27]. The authors claimed they have confirmed that

iodinated analogues of ruthenium anticancer drugs remain intake after cellular uptake by imaging XRF of the cell. Both iodine and ruthenium distribution maps of the cell matched, proving that the drugs are intact to the cell.

XRF reports that are introduced so far have used high flux synchrotron source. As the source has such small beam diameter at high flux, damages to samples are inevitable. N. Manohar et al. (2016) reported a quantitative imaging study of gold nanoparticle distribution in a mouse using benchtop X-ray source [28]. Through their postmortem study, capabilities of XFCT to image spatial distribution of gold nanoparticle and to determine concentration of nonradioactive metallic probes were demonstrated. As gold has relatively high K-alpha energies ($K_{\alpha 1}$ = 68.8 keV, and $K_{\alpha 2}$ = 67 keV) of X-ray fluorescence, penetration depths of the signal were largely increased. According to the authors, metal detection limit of their system is reported as 0.24 wt%.

2.5 X-ray Induced Photodynamic Therapy (XPDT) and XPDT Nanoparticles

Treatments of disease with light have a long history starting from ancient Egyptians treating skin disease called vitiligo [L.B. Josefsen and R.W. Boyle 2008] [29]. Studies on treatment of cancer via conventional PDT started in the early twentieth century Munich by H. Von Tappeiner and A. Jesionek (1905) [30]. Studies and developments of photosensitizers have attracted many interests with hopes to conquer different types of disease such as head and neck cancer, wet type macular degeneration, and bladder cancer [R.R. Allison et al. 2004] [31]. At the current stage of PDT developments, there are two hurdles the treatment technique must overcome: short radius action of photosensitizers, and lack of treatment efficacies due to short penetration depth of light source.

Radiation therapy has been widely used to treat cancer no matter which stage the tumor is according to the report on “cancer treatment and survivorship statistics” [K. D. Miller et al. 2016] [32]. Enhanced radiotherapy with photosensitizer-coupled nanoscintillator has attracted much attention for increased efficacy of treating cancer. The key to increasing treatment efficiency is the generation of reactive oxygen species such as singlet oxygen, hydroxyl radical, peroxides, and superoxide induced by radiation.

Y. Liu et al. (2008) reported synthesis of $LaF_3:Tb^{3+}$ coupled with meso-tetra(4-carboxyphenyl) porphine (MTCP) to induce X-ray induced PDT [33]. For detection of singlet oxygen, anthracenedipropionic acid (ADPA) was used. Absorption spectrum of MTCP was well-

matched with emission spectrum of $LaF_3:Tb^{3+}$, which increases singlet oxygen yield of MTCP. This study has shown XPDT may be possible to deep-seated tumors under ionizing radiation.

A. Bulin et al. (2013) reported synthesis of Tb_2O_3 covered by a polysiloxane layer coupled to porphyrin and characterization of the coupled nanoparticles [34]. The estimated ratio between nanoparticle and photosensitizer molecules was around 1:13. Two commercial probes were used to detect reactive oxygen species. 3'-p-(aminophenyl)fluorescein (APF) and singlet oxygen sensor green (SOSG) were used to detect hydroxyl radical and singlet oxygen respectively.

Table 2.1: Different nanoparticles conjugates for XPDT

	Nanoscintillator	Photosensitizer	ROS Detector	X-ray Energy (Dose Rate)
Y. Liu et al. (2008)	$LaF_3:Tb^{3+}$	MTCP	ADPA	250 keV (0.44Gy/min)
A. Bulin et al. (2013)	Tb_2O_3	Porphyrin	APF and SOSG	44 kV (5.4 mGy/s)
S. Kascakova et al. (2015) [35]	GdEuC12	Hypericin derivatives	Mass Spectrometry	12 kV (NA)
H. Chen et al. (2015) [36]	$SrAl_2O_4:Eu^{2+}$	Merocyanine540	SOSG	40 kV (1 Gy/hr)
Y. Tang et al. (2015) [37]	$LaF_3:Tb^{3+}$	RB	DPBF	75 kV (NA)
L. Ma et al. (2016) [38]	ZnS:Ag,Co	PPIX	NA	120kV, 250kV (NA)

Chapter 3: Materials and Methods

This chapter describes what procedures were followed to build system, check system, and perform the experiments. As this works presents a unique imaging technique, a hybrid system of XF/XL/CT was developed. QDs as XL nanoprobes were characterized with UV/VIS spectrometer for visible light spectrum as well as CdTe spectrometer for X-ray spectrum. For mimicking light absorbing properties of tissue, silicon optical phantom fabrication method is described.

3.1 Dark Box

The hybrid system involves few photon-sensitive elements such as cameras, and spectrometer. To block ambient visible photon as well as cosmic X-ray, the benchtop hybrid XF/XL/CT system is placed in a light-tight box with metric optical table. Black electrical tapes as well as black lining sponges were attached to small holes and gaps that may let photons penetrate through. To block ambient visible light penetrating through top of the box, black turf was attached. Also, thick walls of the dark box prevent researchers from getting exposed to high energy radiation source such as X-ray.

Figure 3.1 The dark box and black turf on top.

3.2 X-ray Source

Two sources of X-ray are present in the dark box. (1) Xenocs' Genix 3D is a high flux monochromatic X-ray source that has peak emission energy of 17.48 keV with tunable beam size and tunable flux. The monochromatic source also features source shutter that can be controlled by computer. (2) Oxford Instrument's Apogee 5000 is a polychromatic source that has emission energy ranging from 10 keV to 50 keV. The beam size of polychromatic source can be tuned by Tungsten pinhole that has a wide range of sizes (100 μm to 2.5cm in diameter). The polychromatic source features computer-controlled tube voltage and tube current. Copper encased shutter is

attached to the polychromatic source so that users can control timing of the X-ray beam. Copper is encased around the shutter to prevent infrared photons that are generated in a shutter from interrupting nanoprobes as well as cameras.

3.3 XL Detection System

The XL detection system originates from an intensified EMCCD camera detection system for low energy Gamma ray imaging [39]. As the low-energy Gamma camera requires sensitive detection system, it is also suitable to detect weak XL signal.

3.3.1 EMCCD: X-ray Luminescence Detection System

Basis of XL detection is an electron-multiplying charge-coupled device (EMCCD). Andor's iXon 3 997 was used as EMCCD camera based on Silicon sensor. The pixel size of the camera is 16 μm x 16 μm, making the intrinsic spatial resolution to be 16 micrometers without any optical instruments attached. The camera has 512 x 512 pixels. In order to increase sensitivity of the camera, electron-multiplying (EM) gain can be modified. XL signal can be weakly emissive (few thousands of photons per interaction) so EM gain must be modified depending on yield of XL nanoprobes that are tested. As EM gain increases, not only signal increases but also noise increases. Hence, optimizing the camera with different settings such as horizontal shift speed, vertical pixel speed, pre-amplifier gain, frame transfer, exposure time, and vertical clock voltage is essential. For each setting, there is a tradeoff between signal and noise, making users to quantify signal and noise properly. To reduce effects of dark noise, water-cooling system is integrated into the system. New generation of Andor's EMCCD can go below -80 ºC because the sensor is encapsulated in vacuum, blocking heat being transferred. The EMCCD used in this study can reach below -35 ºC as there is no air-tight vacuum chamber for better cooling.

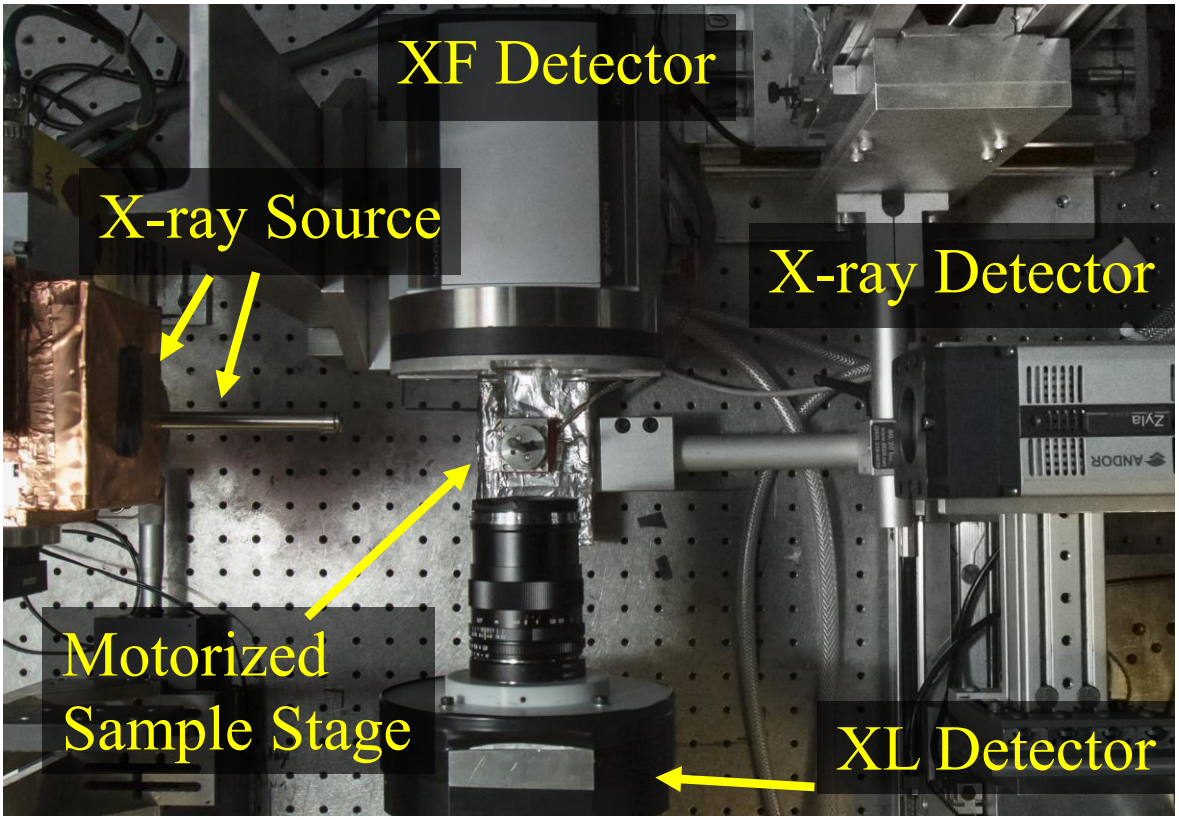

Figure 3.2 Top-down view of the hybrid system.

3.3.2 Intensified EMCCD

To increase visible photon detection sensitivity, Photek's demagnifier (DM) tube is attached to the surface of EMCCD sensor [39]. Using a demagnifier with an active area of 80 mm in diameter helps increasing sensitivity in two ways. Sensitivity of DM tube maximizes at 400nm - 500nm while silicon sensor's spectral response peaks at 900nm – 1000nm. Captured photons are transferred to photocathode that is present at the front window of the DM tube and multiplied into electrons. The photon-generated electrons then converge into the phosphor screen and are re-converted into photons. In turn, multiplied photons are generated and enter EMCCD sensor readout, enhancing sensitivity of XL detection system. With DM tube attached, the resolution of intensified EMCCD (I-EMCCD) is measured with back-lighted United States Air Force (USAF) resolution test target. Magnification ratio of the DM tube is 1:4 (object : image). To make light-tight environment of DM tube, special anodized aluminum casing is encased around the DM tube.

3.3.3 I-EMCCD with Optical Filter

To collect XL signal that is generated by the XL nanoprobes, fluorescence bandpass optical filter is attached in front of DM tube. The optical filter has 50 mm diameter glass window. 3D printed filter adapter that holds the optical filter to DM tube was prepared. For effective filtering of XL signal from the nanoprobes, UV/VIS spectrometer was used to measure the emission wavelengths. Based on the emission wavelength information, the bandwidth as well as the peak wavelength of bandpass filter was chosen.

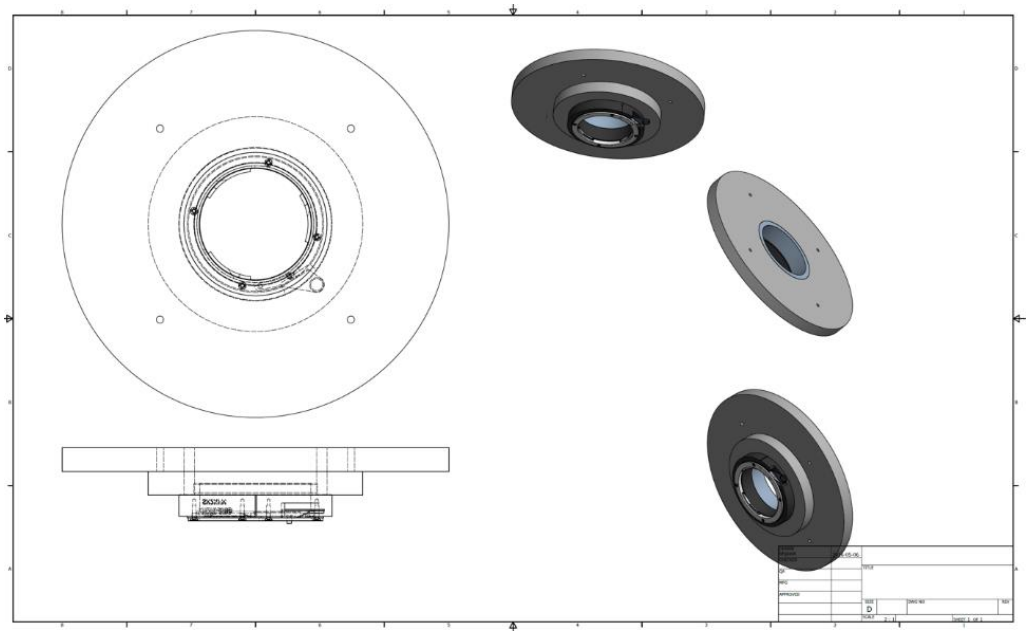

Figure 3.3 Drawing of lens adapter design.

3.3.4 I-EMCCD with Optical Lens

I-EMCCD by itself has very short working distance, which is less than 1 cm. By integrating optical lens system to I-EMCCD, users may change distance between sample stage and I-EMCCD with more degrees of freedom. Due to limited space of dark box, lens (Zeiss classic distagon T* 2.8/25) with shortest focusing distance is chosen. Diameter of the image field for this lens is 43 mm, which is enough for full coverage of DM tube effective area. Among commercially-available

lens that has short focusing distance, Zeiss's lens has the largest aperture size (F-number = 2.8), which is extremely important for capturing low-light condition.

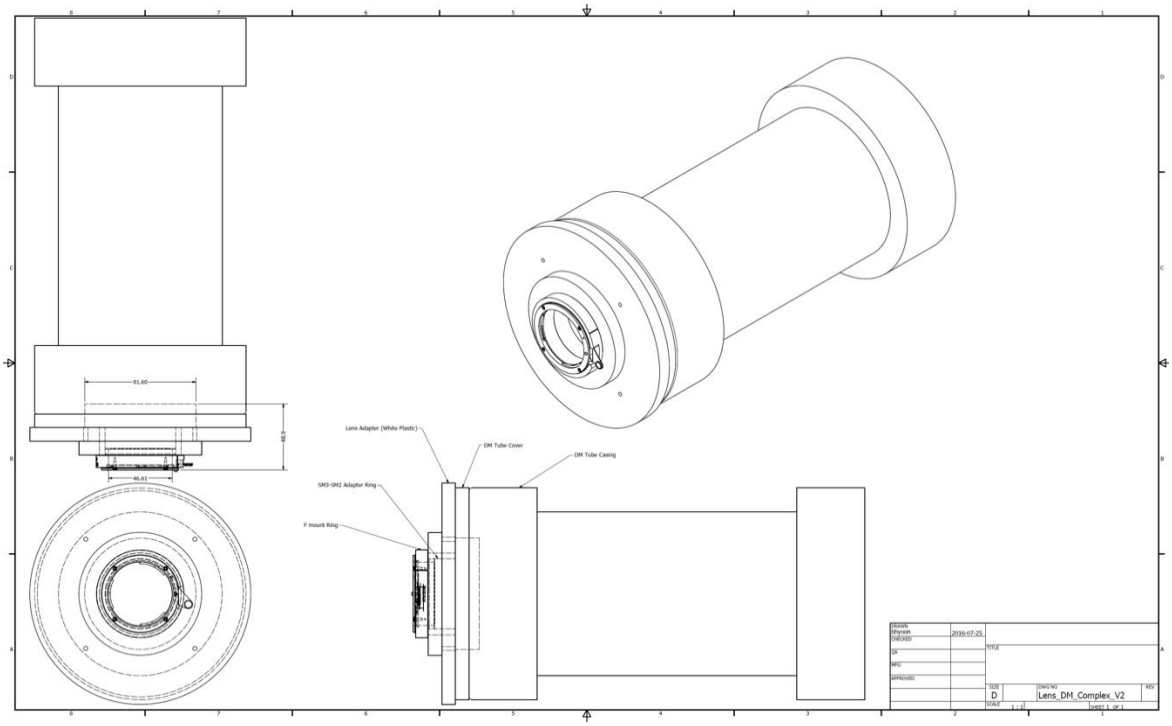

Figure 3.4 Drawing of assembled lens adapter and demagnifier tube.

At the smallest focusing distance, the field of view is at 55 mm x 83 mm and magnification ratio is at 1:2.3 (image : object). For attachment of the optical lens to DM tube casing, depth of DM tube from the frontal surface of the tube casing is measured. As the lens is Nikon's F-mount, the flange distance (distance between lens bayonet and surface of DM tube) is at 46.5 mm. Finally, 3D printed lens adapter must have extrusion length which is the subtracted value between flange distance and depth of DM tube. Extension sliding ring is implemented into the adapter so that flange distance can be accurately modified. For accurate modification of flange distance, back-lighted USAF target is placed in front of the lens at working distance and the extension sliding ring is moved back and forth until the best image resolution is achieved.

3.3.5 Data Acquisition and Processing of XL

The response of EMCCD drifts over time as acquisition time of XL increases. To compensate the drifting effect, reference and experimental data are acquired so that they intersect

each other. For example, 60 frames of background/reference are taken and 60 frames of experiment data are acquired consecutively. The acquisition processes are automatically controlled by computer by opening and closing source shutter of the X-ray source.

Processing of the XL background/reference and experimental data first (a) goes through pedestal calculation which computes average background level of each pixel in arbitrary digital unit (ADU). After the initial pedestal calculation, (b) the subtraction between signal and initial pedestal frame occurs. Subtracted data then goes through (c) a second order pedestal correction which counts number of pixels that fall through set pedestal range and adds pixel values of pedestal pixels. Lastly, (d) pedestal-corrected frame is averaged and quantified by calculating mean and standard deviation value.

Once pedestal correction is complete, region-of-interest (ROI) setting is determined, depending on how signal image looks like. Mean of the signal is then calculated within the ROI.

3.4 XF Detection System [40]

3.4.1 CCD: X-ray Fluorescence Detection System

Andor's CCD, namely iKon-L, collects XF photons emitted from nanocrystals that contain high Z metals under X-ray irradiation. The camera has similar setting modifications with those of EMCCD but the CCD has slower readout rate overall. Number of pixels are 2048 x 2048 with 13.5 μm x 13.5 μm pixel size. Effective detection energy range of the camera is up to 20 keV. The CCD also uses a water-cooling system that is connected through EMCCD and a water chiller. Temperature of the camera decreases all the way down to -35 ºC.

3.4.2 Slit Aperture and CCD

Slit aperture with 100 μm slit width is attached to the CCD for higher resolution and 3D tomographic imaging. For different magnification ratio of projected XF image, distance between slit aperture and CCD may be modified. Once desired magnification ratio is set, geometrical calibration occurs to ensure that the placement of the CCD is appropriate.

3.5 X-ray Detection System

Andor's Scinentific Complementary Metal-Oxide-Semiconducotr (sCMOS) monitors X-ray photons that proceed from the direction parallel to the X-ray beam from X-ray source. The temperature of the sCMOS decreases to 0 ºC via air-cooling method within relatively short amount of time. Pixel array of the camera is 2560 x 2160 pixels and 6.5 μm of pixel size. The camera uses indirect detection of X-ray via CsI:Tl scintillator in front of CMOS sensor. For blocking of low energy photons such as ultraviolet (UV) or visible light, thin Aluminum plate is attached to the scintillator. 10 line pairs / mm of spatial resolution is reported by Andor [e]. With such high speed and high spatial resolution, the X-ray camera helps aligning small diameter X-ray beam (100 μm) and a sample that is also relatively small (200 μm ~ 1mm).

3.6 Beam Alignment

Alignments between sample and X-ray beam differ between monochromatic X-ray source and polychromatic X-ray source. Beam alignments are conducted by monitoring beam line with a Zyla sCMOS X-ray camera. For the monochromatic X-ray source beam alignment, a sample is put on a sample stage. Then, the sample stage is moved to directions perpendicular to the beam line until the beam is not detected by the X-ray camera. For the polychromatic X-ray source beam alignment, X-ray projection image of the sample is first monitored with the X-ray camera. The projection image can be obtained by removing the pinhole aperture in front of the polychromatic source, making a fan beam of X-ray. Then, mark crosshair on the X-ray camera to guide where pencil beam hits the sample. Once the crosshair marking is done, pinhole aperture is placed in front of the source again. Pinhole aperture may be moved by manual stages that modify beam position that is parallel to the X-ray camera. The pencil beam that passes through the pinhole is then aimed to the crosshair on the X-ray camera.

3.7 Characterization of QDs and Upconversion Nanoparticles

Characterization of nanoparticles was done with two spectroscopic studies: UV/VIS spectroscopy and X-ray spectroscopy. Each spectroscopy was performed using different settings. QDs were fabricated in aqueous form so glass cuvettes were used to characterize UV/VIS

spectrometer. Upconversion nanoparticles were fabricated in powder form, making them challenging to confine in glass cuvettes. Hence, a different container was used for UV/VIS characterization. For X-ray spectroscopic characterization, a transparent plastic container is used to avoid scattering and contamination originating from glass impurities.

3.7.1 UV/Vis Spectrum of Upconversion Nanoparticles

Measurements of upconversion nanoparticles in powder form were performed. To preserve and fix powder in the spectrometer, upconversion nanoparticles were placed on top of glass slide and covered with another glass slide. Tapes were attached to the slides to prevent powder from falling out. The angle of sample position was modified to decrease chance of scattering as the samples were in solid form, known to increase scattering events. Once the optimum sample angle was set, two types of spectra were measured. First, the absorption spectra from different upconversion nanoparticles were measured. Based on the absorption spectra, maximum peak wavelength was chosen. Second, the nanoparticles were excited with the peak wavelength and the emission spectra were recorded. As there are multiple absorption peaks observed for upconversion nanoparticles, different excitation wavelengths were used to scan emission spectra.

3.7.2 X-ray Absorption Spectrum of QDs and Upconversion Nanoparticles

X-ray absorption spectrum is measured with Amptek's CdTe detector. The detector is placed so that it faces towards the X-ray source. To calculate how much X-rays are absorbed in the sample, reference data is acquired by measuring (1) X-ray beam spectrum without any samples. Then, the sample is mounted to the sample stage and (2) the corresponding X-ray spectrum is measured. Finally, subtraction between (1) spectrum data without samples and (2) spectrum data with sample becomes X-ray absorption spectrum of the sample.

To reduce the number of scattering X-ray photons, a pinhole aperture of 100 μm in diameters is placed in front of the CdTe detector so that only the beamline reaches the detector. To make sure the X-ray beam hits the detection area, CdTe detector is translated until the highest count rate is measured.

QDs were prepared in an aqueous form dissolved in Hexane, which is known to dissolve plastic containers. Transparent polypropylene centrifuge tubes with volume of 200 μL are used to measure X-ray absorption spectra of QDs. Following experimental schemes are conducted for measuring the corresponding X-ray absorption spectra: (a) different X-ray tube energies, (b) different X-ray tube current, and (c) different concentrations of QDs.

3.8 Nanoparticles-embedded Optical and XF/XL Phantom

To mimic tissue-like optical properties for realistic modeling of XF and XL, few optical phantoms were fabricated. Agarose and polydimethylsiloxane (PDMS) are known to reproduce refractive index of skin tissue. Here, nanoparticles were embedded in the phantom such that XF and XL signal may penetrate and diffuse through the media. For even more realistic modeling of tissue, scattering and absorbing media were introduced. After fabrication of the phantom, XF and XL imaging of the phantoms were conducted. To avoid XF and XL signal emitted by impurities in glass, plastic micropipette tips with diameter of 700 micrometers were used to confine nanoparticles. Both ends of the tips were sealed by burning them with propane gas lighter.

3.8.1 Fabrication of Agarose Phantom

Agarose-based optical phantom was fabricated to image XL and XF of embedded nanoparticles. Two sets of 1 cm cubic agarose were made and stored in two environments to test durability and optical transparency over time. One phantom was stored in a 250 mL beaker, wrapped with parafilm and placed in 4 ºC refrigerator. The other phantom was stored in a 250 mL beaker filled with PBS 1X buffer, sealed with parafilm and placed in room temperature table. After days of monitoring how agarose-based phantom looks like, different types of materials for the optical phantom were explored.

3.8.2 Fabrication of Polydimethylsiloxane (PDMS) Phantom

Elastosil RT 604 from Wacker Chemie AG was used to make silicon-based optical phantom. A Silicon phantom is suitable for sustaining its shape and concentration over long time. Compared to an Agarose phantom which deteriorates and dehumidifies over time, a PDMS phantom generates rigid, flexible, and transparent matrix that has refractive index of 1.4 [41]. Elastosil RT 604 comes as a kit in two components which are part A for PDMS and part B for curing agent and crosslinker. Part A and part B are mixed with volume of weight ratio of 9:1. For reproducing scattering and absorption properties of tissue, recipe from Ayers et al. [42] was referred. The uncured solution was poured into 1 cm diameter mold after mixing three compounds together. After pouring the solution, the mold was sealed with parafilm. As there is no degassing process involved in this fabrication, air bubbles were constantly generated and popped on the surface of the solution. To accommodate space for the popped air, small holes with diameter of 100 μm were punctured on the parafilm. Finally, plastic micropipette tip filled with nanoparticles was inserted through the parafilm in the middle. Parafilm helps making the tip into upright position and holds it until the gel is completely cured. The gel was cured for 24 hours as the manual says.

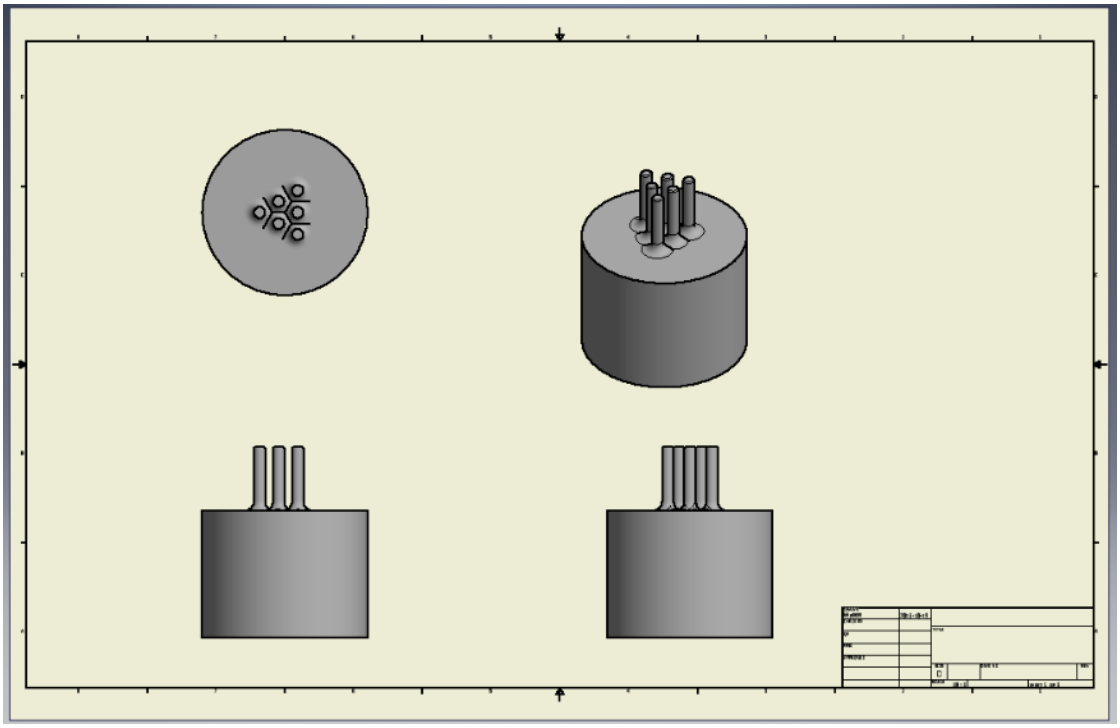

Figure 3.5 Drawing of cast for 9 channel PDMS phantom.

Chapter 4: Results

4.1 Resolving Powers of I-EMCCD and Lens-attached I-EMCCD

Spatial resolution of I-EMCCD and lens-attached I-EMCCD were measured. As I-EMCCD has no focal distance, the USAF target was attached directly to the surface of the demagnifier. Measured spatial resolution of I-EMCCD was at 6.35 line pairs / mm (Group 2, Element 5). With the wide-angle lens (focal length 25 mm) installed, spatial resolution was expected to decrease as magnification ratio is lower than 1 (demagnifying ratio). Measured spatial resolution of lens-attached I-EMCCD was at 2.52 line pairs / mm (Group 1, Element 3).

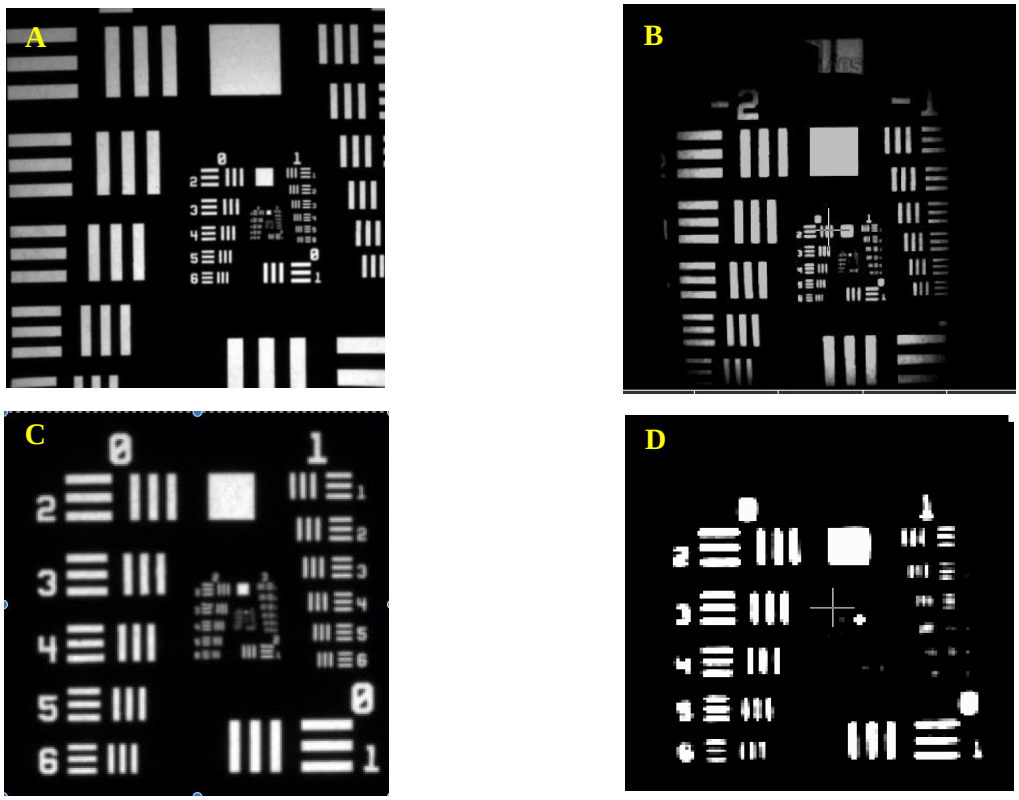

Figure 4.1 (A) Resolution of I-EMCCD. (B) Resolution of Lens-attached I-EMCCD. (C) Resolution of I-EMCCD (expanded). (D) Resolution of Lens-attached I-EMCCD (expanded, high-contrast).

4.2 Temporal Stability Tracking of I-EMCCD

Demagnifier contains a photocathode that requires high voltage source of 10kV. 1000 background frames of four different scenarios were taken to speculate changes of values over time as shown in Table 4.1 : (a) lens is closed and DM tube is off (LensCapOnDMOFF), (b) lens is open and DM tube is off (EM_DMOff), (c) lens is closed and DM tube is on (LensCapOn_DMOn), and (d) lens is open and DM tube is on (EM_DMOn). Frame average and frame standard deviation over number of frames were acquired. For comparison, mean values of each pixel over frames were plotted to ensure values of individual pixels follow the trend of frame averages. During background acquisitions, no known light source was turned on. Electron-multiplying gain was at 2048, which is half of maximum gain. Both mean levels and standard deviation levels of all four scenarios were relatively similar in that differences between the levels are within 1 ADU which is a minimum discernible unit of EMCCD.

Table 4.1: Background levels of EMCCD in different scenarios

Unit: ADU	**Average**	**STD.**	**Min/Max**
EM_DMOff	407.03957	0.07698	406.861 407.285
EM_DMOn	407.11747	0.07708	406.943 407.397
LensCapOnDMOn	406.95814	0.07452	406.779 407.238
LensCapOnDMOFF	406.64009	0.07371	406.409 406.87

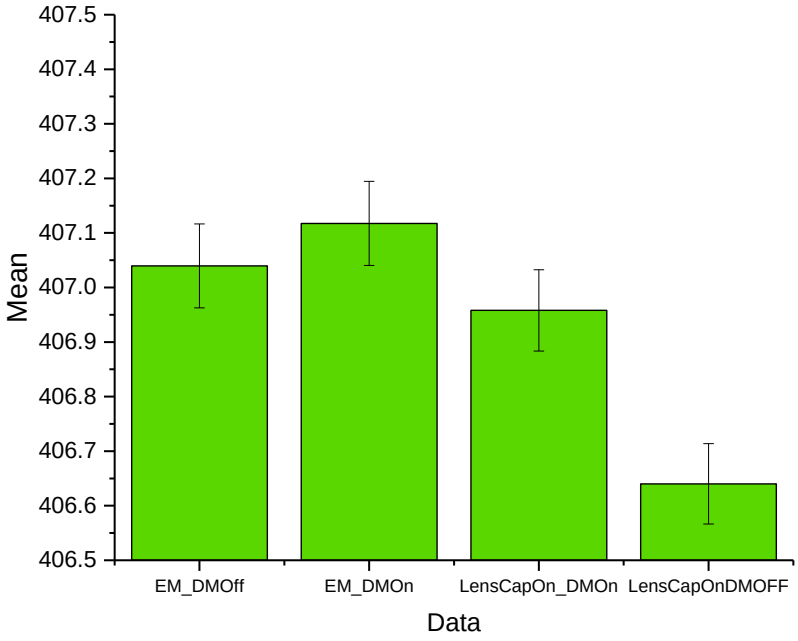

Figure 4.2 Background mean and standard deviation levels for four different scenarios.

4.3 Attenuation and XL of Glass Container

Silica-based quartz and glass products are regularly used as sample containers for many spectroscopic studies such as UV/VIS spectroscopy and nuclear magnetic resonance (NMR) spectroscopy due to their excellent optical transparency and chemical compatibility. Metal oxides and silica glasses are known to generate XEOL, which makes many glass cuvettes and vials to be inappropriate sample containers for testing XEOL of samples as shows in Figure 4.4 [43]. Most of QDs used in this study were diluted in hexane, which notoriously dissolves many types of plastics such as polycarbonate and polystyrene. Hence, high density polyethylene tube of 5 mm in diameter was finally chosen as a sample container.

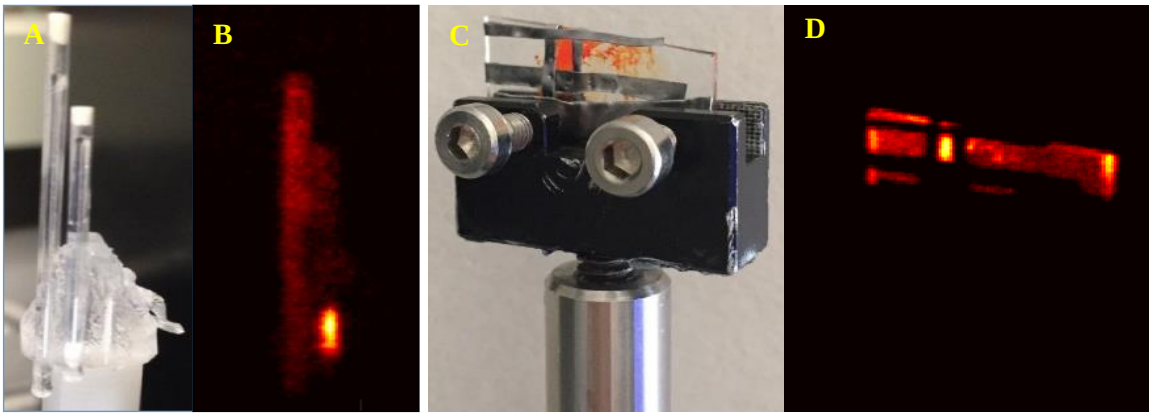

Figure 4.3 Comparisons between different samples. (A) Actual image of LaF_3:Tb^{3+} (left) and Y_2O_3:Eu^{3+} (right) containing mouse phantom. (B) XL of the mouse phantom. Hot spot is the strong XL of Y_2O_3:Eu^{3+}. (C) Drop-casted QD600 on glass slide. Lead tape is attached to confine region of interest. (D) XL of the QD600 on glass slide. Scattered glass XL is observed on the sides of the glass slide.

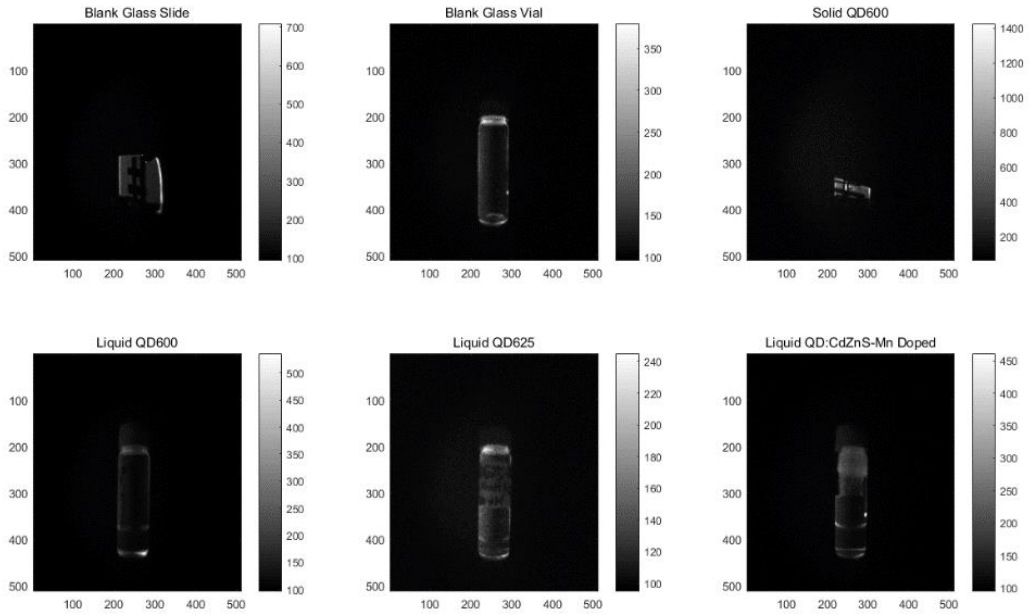

Figure 4.4 XL of glass vials and glass slide. X-ray energy is not efficiently delivered to the sample in the vial due to attenuation of the glass vials.

4.4 Result of Phantom Fabrication

4.4.1 Fabrication of Cylindrical Phantom and Optical Scattering

Two different phantoms were fabricated: one with no scattering medium mixed and the other with scattering medium mixed. Both phantoms had 1mm ~ 2 mm micropipette tip containing QD625 and the tips were sealed via heat treatment. For quality verification prior to actual XL/XF imaging of the phantoms, transmission and diffusion tests were performed with green laser pointer (emission wavelength = 522~ 542 nm). To simulate how the scattered photons will travel under X-ray, handheld blacklight (emission wavelength = 390 ~ 395 nm) was used to irradiate the phantoms. Overall, scattering media showed light diffusion characteristic of the phantoms as shown in Figure 4.5 (D) and Figure 4.5 (E).

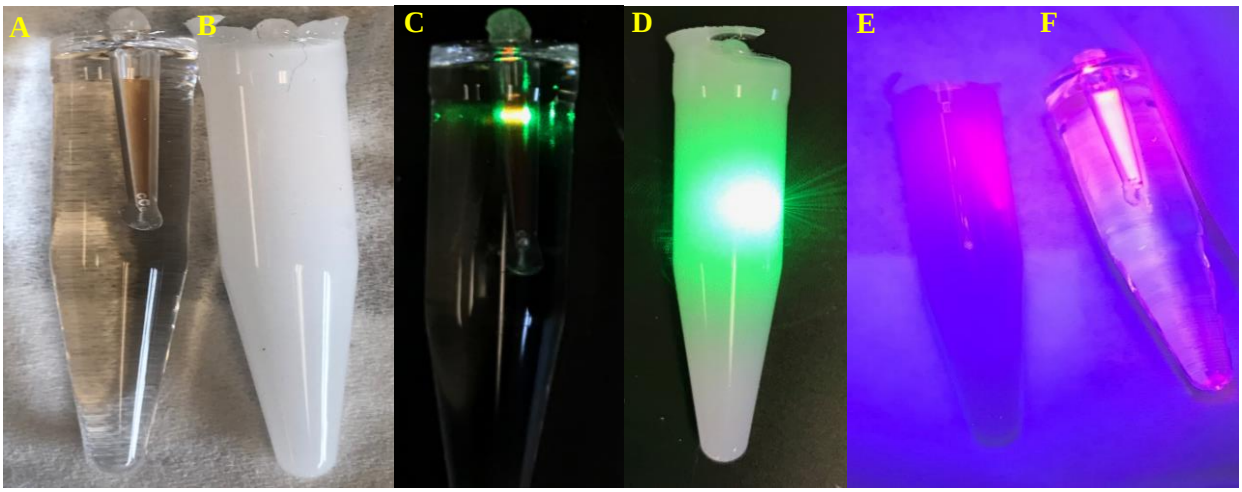

Figure 4.5 (A) PDMS phantom with QD625 in the middle and without scattering medium. (B) PDMS phantom with scattering medium and with QD625 in the middle. (C) Green laser transmission test on PDMS phantom without scattering medium. (D) Green laser diffusion test on PDMS phantom with scattering medium. (E) UV excitation test on PDMS phantom with scattering medium. Diffused optical emission of QD625 was observed. (F) UV excitation test on PDMS phantom without scattering medium.

4.4.2 Fabrication of Cubic Phantom and XL Scattering

PDMS-based phantom was fabricated with 2.2 cm L x 2.2 cm W x 2 cm H ice cube tray. As the cube tray was made of silicone, petroleum gel was applied for surface treatment. The treatment improved release process once the PDMS is fully cured. At the center of the cube, 150 μm cylindrical channel with 2 cm height was made for quick insertion of nanoparticles. XL of the scattering cubic phantom is shows in Figure 4.6 (C).

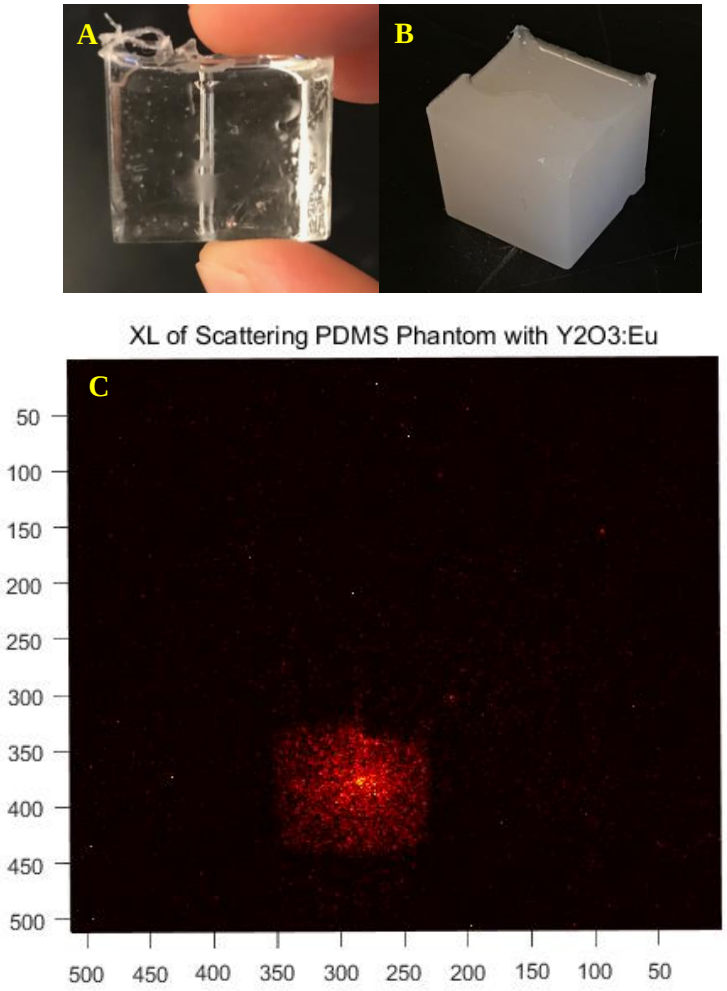

Figure 4.6 (A) PDMS phantom with no scattering media. The cube was fabricated to show location of inner channel. (B) PDMS phantom with scattering medium. The top portion is irregular due to adhesion between gel and parfilm during curing. (C) XL image of scattering PDMS phantom with Y_2O_3:Eu^{3+} nanoparticles in the middle. Red pseuocolor was applied. Bright spot is shown in the middle of the cube.

4.5 Upconversion Nanoparticle UV/VIS Spectra

Electronic energy states of upconversion nanoparticles are peculiar in that there are multiple peaks present in both absorption and emission spectra. As the nanoparticles were in powder forms, angles of sample stage were modified until desired spectra with acceptable signal-to-noise ratio were acquired. Observed major peak of Y_2O_3:Eu^{3+} nanoparticles originates from the Eu-dopant. Emission spectrum of LaF_3:Tb^{3+} yielded relatively noisy data due to its low quantum yield and large scattering events of optical photons.

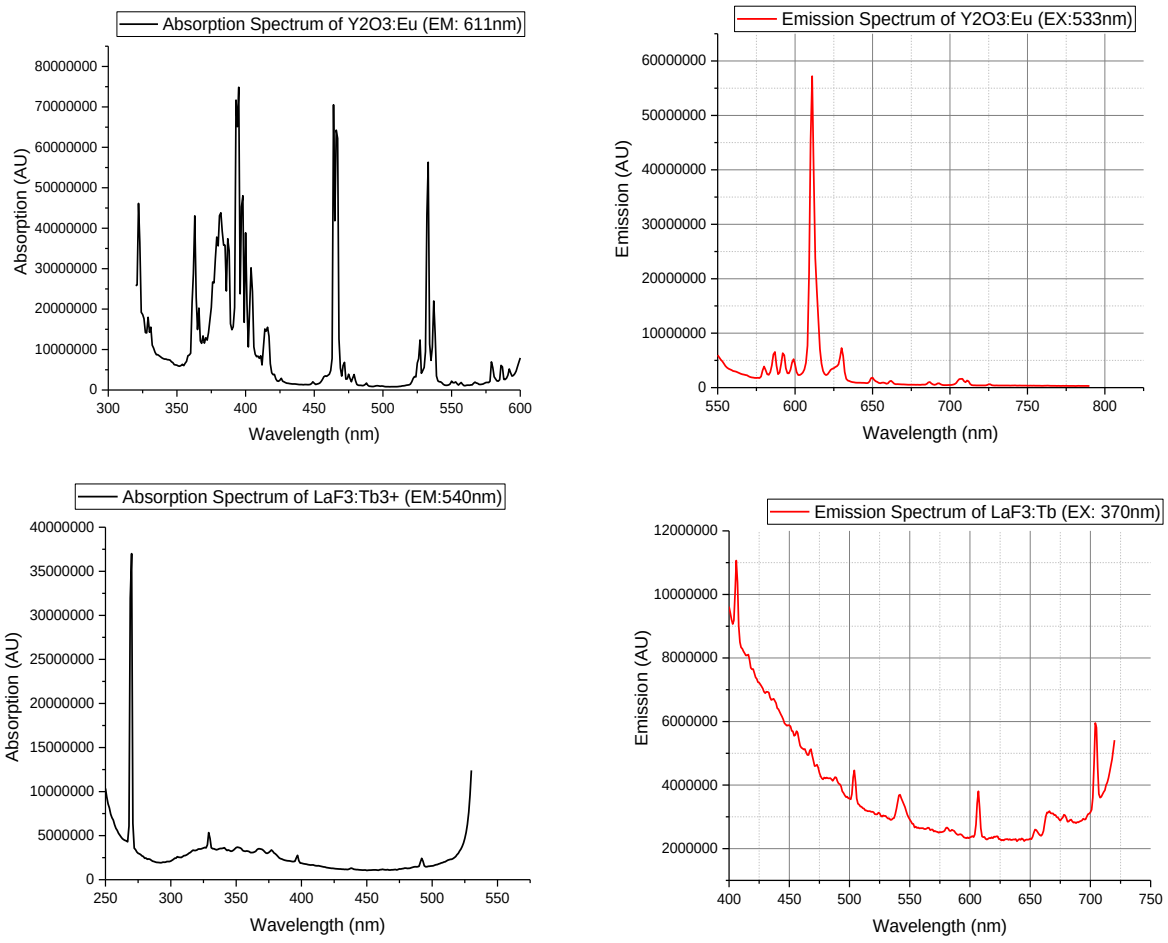

Figure 4.7 Absorption and emission spectra of Y_2O_3:Eu^{3+} and LaF_3:Tb^{3+} nanoparticles.

4.6 XL Image of ZnCdS:Mn QD

The ROI of camera was set to be 64 x 64 pixelsas smaller ROI enables faster signal acquisition, increasing overall sensitivity of the camera. Increasing horizontal pedestal trend over in a frame was observed. This was corrected via subtraction between averaged signal frame and averaged background frame after XL signal processing. Linear shape of the X-ray beampath (5 mm) was well-observed. Position 0 denotes background frame and position 1 denotes signal frame. The sample container was a 5 mm wide microcentrifuge platic tube.

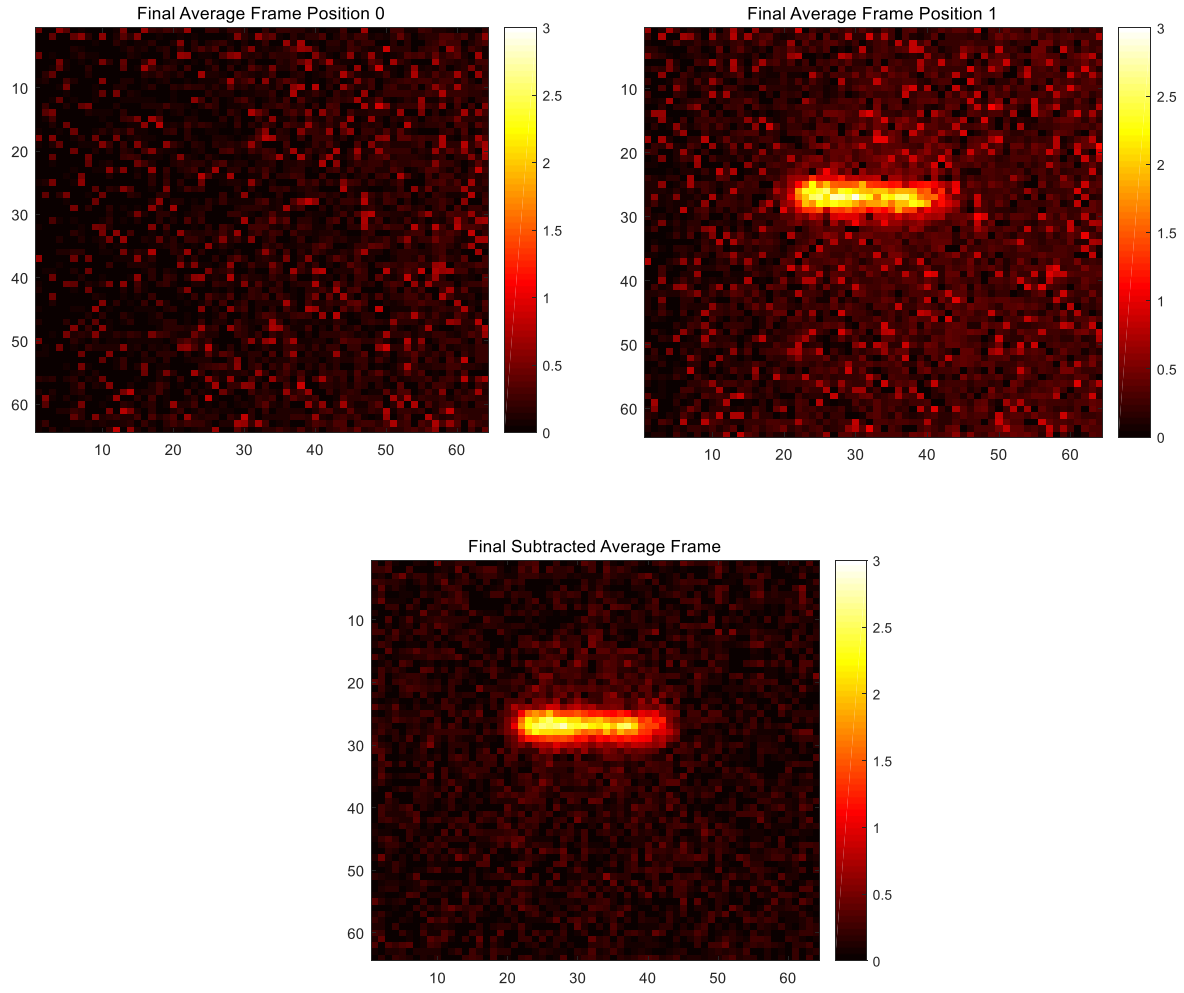

Figure 4.8 Averaged frame of background (position 0), signal (position 1), and subtracted frame. Red pseudocolor colormap was applied.

4.7 XL Quantification of ZnCdS:Mn QD

Following graphs were taken by setting the same area of ROI for each experiment. Overall, XL of ZnCdS:Mn QDs shows increasing trends as X-ray tube voltage increases, X-ray tube current increases, and concentration of QD increases. Both polychromatic and monochromatic X-ray sources show increasing trend.

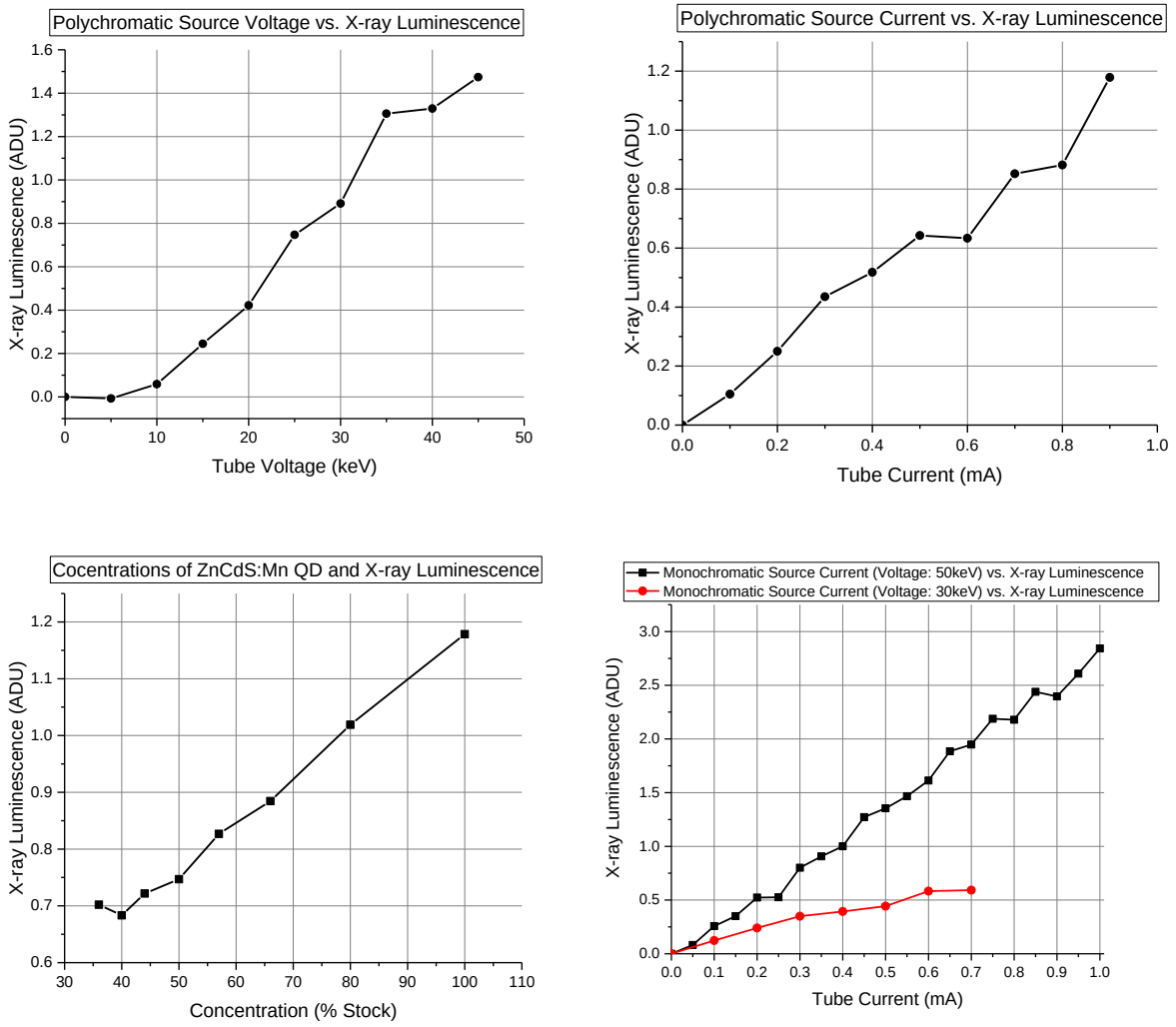

Figure 4.9 XL quantification graphs on different sets of experiments. ZnCdS:Mn QD was used as test sample.

4.8 Superimposed Optical and XL Images of ZnCdS:Mn QD

Overlaying both optical image and XL image helps identifying what beampath looks like, and which portion of sample X-ray irradiates. Figure 4.10 (A) shows the whole view of setup and the ROI was set to be 512 x 512. Location of 64 x 64 ROI was already known. Hence, matching ROI with that in XL frame was zoomed in as shown in figure 4.10 (B). Intensity of XL emitted from QDs largely differs from optical images of setup as shown in figure (C). With multiplication factor that matches with optical intensity shown in Figure 4.10 (B), co-registration between multiplied XL signal and optical signal was conducted (Figure 4.10 (D)).

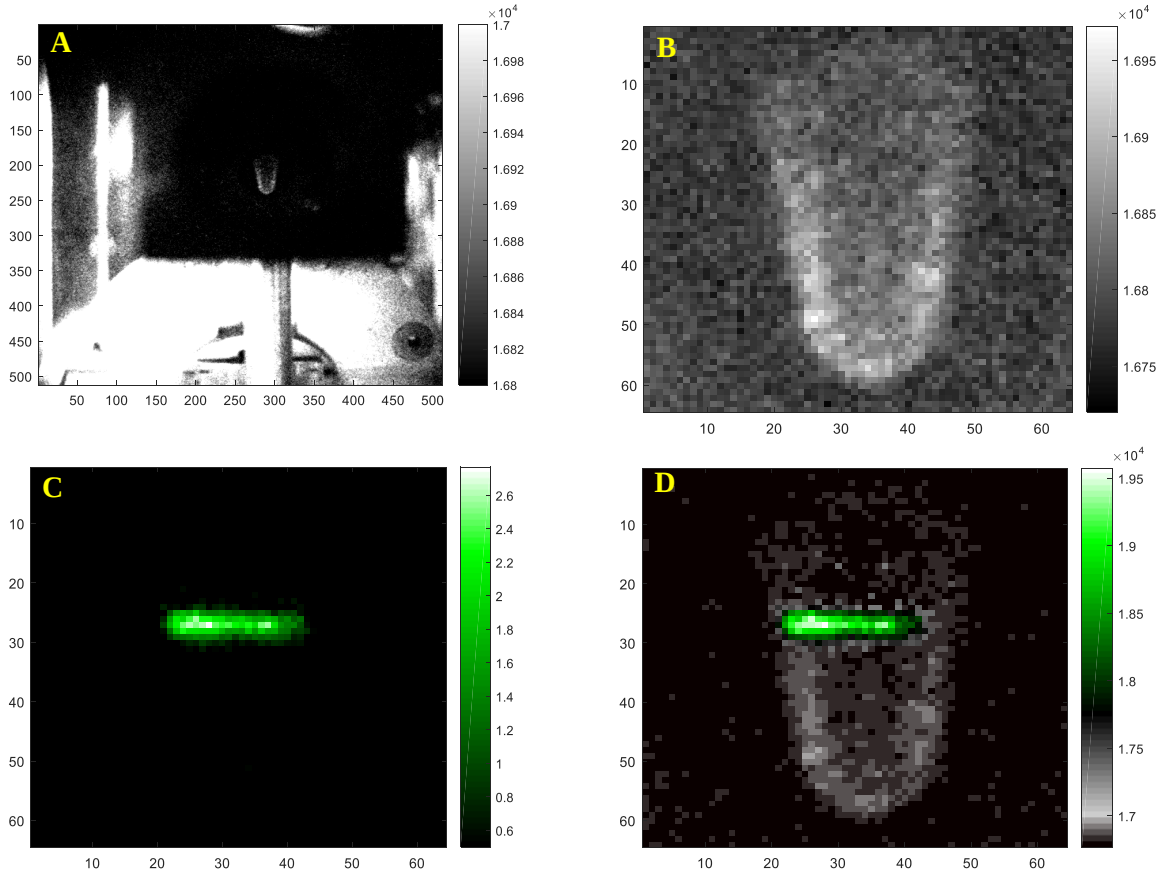

Figure 4.10 Overlay process of optical and XL images. (A) Optical image of the setup with test tube in the middle. (B) Zoomed optical image of the test tube. (C) XL image of stock ZnCdS:Mn QD. Green pseudocolor was applied. (D) Superimposed image of optical and XL images.

Chapter 5: Conclusion

The work in this thesis primarily performs feasibility tests of different nanoparticles on their XL efficiency. Comparisons between XL of un-doped QDs and doped QDs show that there are electron-hole recombination inefficiencies present under high energy excitations. The XL data of ZnCdS:Mn QDs shows it is appropriate to use QDs as a newly-emerging XL nanoprobes. The XL detection system showed exceptional detection efficiency and stability on top of great potentials to increase spatial resolution. Optical phantoms that are composed of PDMS presented strong durability and optical properties that mimic human tissue. Superimposed optical and XL images of QDs showed co-registration of two different signals are possible, foreshowing potentials towards development of hybrid optical fluorescence and XL microscopy. Additionally, diffused XL signal in the scattering PDMS phantom shows XLCT imaging method can be further developed with potentially higher signal-to-noise ratio as the excitation source does not produce any known autofluorescence. Hence, the developed XLCT system as well as Manganese doped ZnCdS QDs are excellent combinations of a new theranostic modality seen as image-guided X-ray photodynamic therapy.

Chapter 6: Discussion and Future Works

There is no doubt that high energy excitation generates many holes and electrons that can potentially recombine and generate visible photons. What is more important than quantifying number of electrons and holes is quantifying how much ratio of generated electrons recombine with holes as a measure of scintillation efficiency. The recombination mechanisms can be studied with detailed spectroscopic studies such as UV/VIS spectroscopy and/or time-resolved photoluminescence. It is certainly possible to quantify the recombined population statistics with different optical filters attached to the current XL detection setup. However, discernible wavelength resolution of spectrometer is distinguishingly better than that of optical filters.

It is also important to track how hot electrons and holes relax down to the band structure before they recombine. In this scheme, measurements of dissipated phonon energies as well as relaxation timing of both electrons and holes would be crucial.

Another parameter that might affect efficiency of XL is the absorption of energy in solvent. Ionized solvent might have enough energy so that the energy transfer to band structure occurs. Electrons that are stripped out of solvent atoms might also be transferred to the band structure, causing recombination to occur. Experimental verifications on energy transfer mechanisms can be verified by robust insulation of nanoparticles with capping agents, suppressing energy transfer between nanoparticles and solvent molecules.

Discrepancies between actual singlet oxygen yield and visible light yield may be present. To accurately determine what is the actual clinical efficacy towards photodynamic therapy, quantification of singlet oxygen per given radiation dose is required. Also, at current stage of the study, it is unknown what is the active volume that singlet oxygen can be diffused through the tumor. In other words, its clinical efficacy might be limited to the peripheral regions of tumor due to lack of singlet oxygen diffusion. However, enhanced radiation therapy combined with photodynamic therapy might have different efficacy, making this study more interesting. Quantification of singlet oxygen can be conducted with incorporation of singlet oxygen sensor green (SOSG) of which emits green fluorescence once the sensor molecule binds to the singlet oxygen. SOSG requires light source to be present as an excitation source. Hence, chemical and photophysical complications among nanoparticles, SOSG, and solvents might occur so different experimental sets with different conditions are required for careful studies of singlet oxygen

generation. For example, filtering optical signal that is purely from fluorescence of SOSG would be crucial. If the emission wavelengths of nanoparticles overlap emission wavelengths of SOSG, optical filter that blocks fluorescence of the nanoparticles is needed. Figure 6.1 shows how singlet oxygen quantification system would look like.

There are other ways to detect and to quantify singlet oxygen with higher accuracy such as singlet oxygen phosphorescence, electron spin resonance, and mass spectrometry. However, the last two methods require extremely bulky detection system, which is not ideal for current X-ray system setup. Also, phosphorescence of singlet oxygen is relatively weak, making phosphorescence quantum efficiency to be low [44]. Therefore, it is reasonable to use singlet oxygen detecting fluorescein for fast and relatively accurate measurements of such reactive oxygen species.

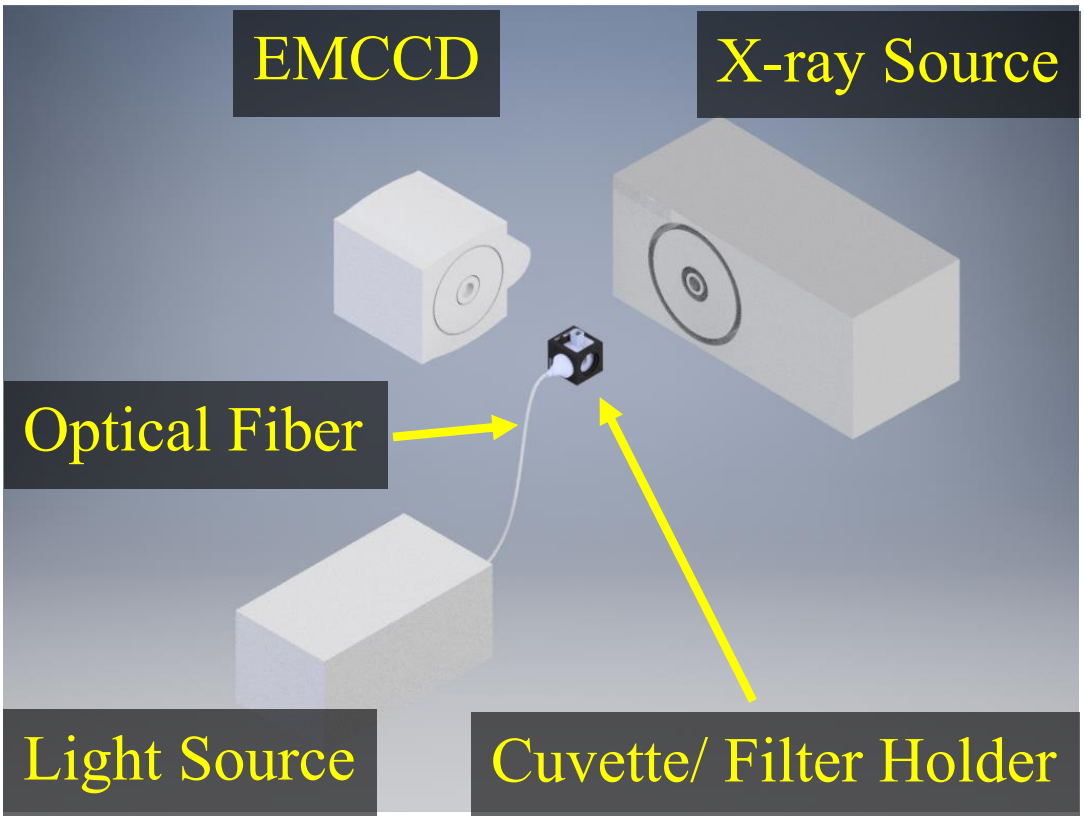

Figure 6.1 Singlet oxygen detection system for quantitative assessments of X-ray photodynamic therapy.

References

[1] K. Doi, "Diagnostic imaging over the last 50 years: research and development in medical imaging science and technology," *Phys Med Biol,* vol. 51, no. 13, pp. R5-27, Jul 07 2006.

[2] "4, The Frequency of Bone Disease," in *Bone Health and Osteoporosis: A Report of the Surgeon General.*Rockville (MD): Office of the Surgeon General (US), 2004.

[3] G. Ingram and N. Munro, "The use (or otherwise) of pulse oximetry in general practice," (in eng), *Br J Gen Pract,* vol. 55, no. 516, pp. 501-2, Jul 1 2005.

[4] S. R. Arridge and J. C. Hebden, "Optical imaging in medicine: II. Modelling and reconstruction," (in eng), *Phys Med Biol,* vol. 42, no. 5, pp. 841-53, May 1997.

[5] P. Agostinis *et al.*, "Photodynamic therapy of cancer: An update," *CA: A Cancer Journal for Clinicians,* vol. 61, no. 4, pp. 250-281, 2011.

[6] L. J. Meng, N. Li, and P. J. L. Riviere, "X-Ray Fluorescence Emission Tomography (XFET) With Novel Imaging Geometries— A Monte Carlo Study," *IEEE Transactions on Nuclear Science,* vol. 58, no. 6, pp. 3359-3369, 2011.

[7] M.C.Miller, *X-Ray Fluorescence* (Passive nondestructive assay manual - PANDA). 2007.

[8] M. Nikl, "Scintillation detectors for x-rays," (in English), *Measurement Science and Technology,* vol. 17, no. 4, pp. R37-R54, Apr 2006.

[9] P. Harrison and A. Valavanis, Quantum wells, wires and dots : theoretical and computational physics of semiconductor nanostructures, Fourth edition. ed., p. 1 online resource. [Online]. Available: Wiley Online Library - Full text http://www.library.illinois.edu/proxy/go.php?url=http://dx.doi.org/10.1002/9781118923337.

[10] Z. Kang *et al.*, "CdTe quantum dots and polymer nanocomposites for x-ray scintillation and imaging," *Appl Phys Lett,* vol. 98, no. 18, p. 181914, May 2 2011.

[11] A. I. Ekimov, "Quantum size effect in three-dimensional microscopic semiconductor crystals," *JETP Letters,* vol. 34, no. 6, p. 345, 1981.

[12] A. M. Smith, H. Duan, A. M. Mohs, and S. Nie, "Bioconjugated quantum dots for in vivo molecular and cellular imaging," *Advanced Drug Delivery Reviews,* vol. 60, no. 11, pp. 1226-1240, 8/17/ 2008.

[13] S. E. Letant and T. F. Wang, "Semiconductor quantum dot scintillation under gamma-ray irradiation," (in eng), *Nano Lett,* vol. 6, no. 12, pp. 2877-80, Dec 2006.

[14] S. E. Létant and T. F. Wang, "Study of porous glass doped with quantum dots or laser dyes under alpha irradiation," *Applied Physics Letters,* vol. 88, no. 10, p. 103110, 2006.

[15] M. Hossu, Z. Liu, M. Yao, L. Ma, and W. Chen, "X-ray luminescence of CdTe quantum dots in LaF3:Ce/CdTe nanocomposites," *Applied Physics Letters,* vol. 100, no. 1, p. 013109, 2012.

[16] W. G. Lawrence, S. Thacker, S. Palamakumbura, K. J. Riley, and V. V. Nagarkar, "Quantum Dot-Organic Polymer Composite Materials for Radiation Detection and Imaging," *IEEE Transactions on Nuclear Science,* vol. 59, no. 1, pp. 215-221, 2012.

[17] G. Gaur *et al.*, "Influence of Ionizing Radiation and the Role of Thiol Ligands on the Reversible Photodarkening of CdTe/CdS Quantum Dots," *ACS Applied Materials & Interfaces,* vol. 8, no. 12, pp. 7869-7876, 2016/03/30 2016.

[18] V. I. Klimov, D. W. McBranch, C. A. Leatherdale, and M. G. Bawendi, "Electron and hole relaxation pathways in semiconductor quantum dots," *Physical Review B,* vol. 60, no. 19, pp. 13740-13749, 11/15/ 1999.

[19] "Multicarrier Interactions in Semiconductor Nanocrystals in Relation to the Phenomena of Auger Recombination and Carrier Multiplication," *Annual Review of Condensed Matter Physics,* vol. 5, no. 1, pp. 285-316, 2014.

[20] L. A. Padilha, W. K. Bae, V. I. Klimov, J. M. Pietryga, and R. D. Schaller, "Response of semiconductor nanocrystals to extremely energetic excitation," *Nano Lett,* vol. 13, no. 3, pp. 925-32, Mar 13 2013.

[21] G. Pratx, C. M. Carpenter, C. Sun, and L. Xing, "X-Ray Luminescence Computed Tomography via Selective Excitation: A Feasibility Study," *IEEE Transactions on Medical Imaging,* vol. 29, no. 12, pp. 1992-1999, 2010.

[22] D. Chen *et al.*, "Cone beam x-ray luminescence computed tomography: a feasibility study," (in eng), *Med Phys,* vol. 40, no. 3, p. 031111, Mar 2013.

[23] D. Chen, S. Zhu, X. Cao, F. Zhao, and J. Liang, "X-ray luminescence computed tomography imaging based on X-ray distribution model and adaptively split Bregman method," *Biomed Opt Express,* vol. 6, no. 7, pp. 2649-63, Jul 1 2015.

[24] S. Corezzi *et al.*, "Synchrotron-based X-ray fluorescence imaging of human cells labeled with CdSe quantum dots," (in eng), *Anal Biochem,* vol. 388, no. 1, pp. 33-9, May 01 2009.

[25] E. Vergucht *et al.*, "In vivo X-ray elemental imaging of single cell model organisms manipulated by laser-based optical tweezers," *Scientific Reports,* Article vol. 5, p. 9049, 03/12/online 2015.

[26] L. Finney *et al.*, "X-ray fluorescence microscopy reveals large-scale relocalization and extracellular translocation of cellular copper during angiogenesis," *Proceedings of the National Academy of Sciences,* vol. 104, no. 7, pp. 2247-2252, February 13, 2007 2007.

[27] S. Antony *et al.*, "X-ray fluorescence imaging of single human cancer cells reveals that the N-heterocyclic ligands of iodinated analogues of ruthenium anticancer drugs remain coordinated after cellular uptake," *JBIC Journal of Biological Inorganic Chemistry,* journal article vol. 18, no. 7, pp. 845-853, 2013.

[28] N. Manohar, F. J. Reynoso, P. Diagaradjane, S. Krishnan, and S. H. Cho, "Quantitative imaging of gold nanoparticle distribution in a tumor-bearing mouse using benchtop x-ray fluorescence computed tomography," *Scientific Reports,* Article vol. 6, p. 22079, 02/25/online 2016.

[29] L. B. Josefsen and R. W. Boyle, "Photodynamic therapy and the development of metal-based photosensitisers," (in eng), *Met Based Drugs,* vol. 2008, p. 276109, 2008.

[30] J. A. V. T. H, "Zur behandlung der Hautcarcinome mit fluorescierenden Stoffen," *Arch. Klin. Med.,* vol. 82, p. 223, 1905.

[31] R. R. Allison, G. H. Downie, R. Cuenca, X. H. Hu, C. J. Childs, and C. H. Sibata, "Photosensitizers in clinical PDT," (in eng), *Photodiagnosis Photodyn Ther,* vol. 1, no. 1, pp. 27-42, May 2004.

[32] K. D. Miller *et al.*, "Cancer treatment and survivorship statistics, 2016," *CA: A Cancer Journal for Clinicians,* vol. 66, no. 4, pp. 271-289, 2016.

[33] Y. Liu, W. Chen, S. Wang, and A. G. Joly, "Investigation of water-soluble x-ray luminescence nanoparticles for photodynamic activation," *Applied Physics Letters,* vol. 92, no. 4, p. 043901, 2008.

[34] A.-L. Bulin *et al.*, "X-ray-Induced Singlet Oxygen Activation with Nanoscintillator-Coupled Porphyrins," *The Journal of Physical Chemistry C*, vol. 117, no. 41, pp. 21583-21589, 2013.

[35] S. Kaščáková *et al.*, "X-ray-induced radiophotodynamic therapy (RPDT) using lanthanide micelles: Beyond depth limitations," *Nano Research*, vol. 8, no. 7, pp. 2373-2379, 2015.

[36] H. Chen *et al.*, "Nanoscintillator-mediated X-ray inducible photodynamic therapy for in vivo cancer treatment," *Nano Lett*, vol. 15, no. 4, pp. 2249-56, Apr 8 2015.

[37] Y. Tang, J. Hu, A. H. Elmenoufy, and X. Yang, "Highly Efficient FRET System Capable of Deep Photodynamic Therapy Established on X-ray Excited Mesoporous LaF3:Tb Scintillating Nanoparticles," *ACS Appl Mater Interfaces*, vol. 7, no. 22, pp. 12261-9, Jun 10 2015.

[38] M. Lun, Z. Xiaoju, H. Marius, and C. Wei, "Synthesis of ZnS:Ag,Co water-soluble blue afterglow nanoparticles and application in photodynamic activation," *Nanotechnology*, vol. 27, no. 31, p. 315602, 2016.

[39] L. J. Meng, G. Fu, E. J. Roy, B. Suppe, and C. T. Chen, "An Ultrahigh Resolution SPECT System for I-125 Mouse Brain Imaging Studies," *Nuclear instruments & methods in physics research. Section A, Accelerators, spectrometers, detectors and associated equipment*, vol. 600, no. 1, pp. 498-505, 2009.

[40] A. Groll, J. George, P. Vargas, P. J. L. Rivière, and L. J. Meng, "Element Mapping in Organic Samples Utilizing a Benchtop X-Ray Fluorescence Emission Tomography (XFET) System," *IEEE Transactions on Nuclear Science*, vol. 62, no. 5, pp. 2310-2317, 2015.

[41] B. W. Pogue and M. S. Patterson, "Review of tissue simulating phantoms for optical spectroscopy, imaging and dosimetry," (in eng), *J Biomed Opt*, vol. 11, no. 4, p. 041102, Jul-Aug 2006.

[42] F. Ayers, A. Grant, D. Kuo, D. J. Cuccia, and A. J. Durkin, "Fabrication and characterization of silicone-based tissue phantoms with tunable optical properties in the visible and near infrared domain," 2008, vol. 6870, pp. 687007-687007-9.

[43] I. Masashi, Y. Tomoko, and S. Kenji, "X-ray excited 3.2 eV luminescence from amorphous silica: radiative electron relaxation through an unidentified centre and its

thermal switching," *Journal of Physics: Condensed Matter,* vol. 20, no. 25, p. 255249, 2008.

[44] J. W. Snyder, E. Skovsen, J. D. C. Lambert, L. Poulsen, and P. R. Ogilby, "Optical detection of singlet oxygen from single cells," *Physical Chemistry Chemical Physics,* 10.1039/B609070M vol. 8, no. 37, pp. 4280-4293, 2006.